NASA Technical Memorandum 4413

Experimental Aerodynamic Characteristics of a Generic Hypersonic Accelerator Configuration at Mach Numbers 1.5 and 2.0

Ira J. Walker, Peter F. Covell,
and Dana K. Forrest

FEBRUARY 1993

NASA Technical Memorandum 4413

Experimental Aerodynamic Characteristics of a Generic Hypersonic Accelerator Configuration at Mach Numbers 1.5 and 2.0

Ira J. Walker
Lockheed Engineering & Sciences Company
Hampton, Virginia

Peter F. Covell and Dana K. Forrest
Langley Research Center
Hampton, Virginia

Summary

An experimental investigation of the static longitudinal and lateral-directional aerodynamic characteristics of a generic hypersonic research vehicle was conducted in the Langley Unitary Plan Wind Tunnel (UPWT). A parametric study was performed to determine the interference effects of various model components. Configuration variables included delta and trapezoidal canards; large and small centerline-mounted vertical tails, along with a set of wing-mounted vertical tails; and a set of model noses with different degrees of bluntness. Wing position was varied by changing the longitudinal location and the incidence angle. The test Mach numbers were 1.5 and 2.0 at Reynolds numbers of 1×10^6 per foot, 2×10^6 per foot, and 4×10^6 per foot. Angle of attack was varied from $-4°$ to $27°$, and sideslip angle was varied from $-8°$ to $8°$.

Generally, the effect of Reynolds number did not deviate from conventional trends. The longitudinal stability and lift-curve slope decreased with increasing Mach number. As the wing was shifted rearward, the lift-curve slope decreased and the longitudinal stability increased. Also, the wing-mounted vertical tails resulted in a more longitudinally stable configuration. In general, the lift-drag ratio was not significantly affected by vertical-tail arrangement. The best lateral-directional stability was achieved with the large centerline-mounted tail, although the wing-mounted vertical tails exhibited the most favorable characteristics at the higher angles of attack.

Introduction

Significant research efforts have been devoted to single-stage-to-orbit hypersonic concepts that could serve as test beds for the development of a trans-atmospheric vehicle (TAV). Achievement of this goal requires innovations in three critical areas: (1) propulsion, (2) materials and structures (including provisions for airframe cooling), and (3) external aerodynamics (ref. 1). Research on this class of vehicles led to the National Aero-Space Plane (NASP) program in the 1980's. As part of the NASP program, several concepts have been investigated, originating both from the National Aeronautics and Space Administration (NASA) and from private industry.

This study examines the effects of various configuration parameters on the aerodynamic characteristics of a generic wing-cone vehicle at low supersonic speeds. The conical forebody serves as an effective precompression ramp for ramjet/scramjet operations. Another advantage of this concept is the simplicity of the geometry, which makes it amenable to analysis by several available computational methods.

This investigation was conducted to evaluate the longitudinal and lateral-directional stability over a range of angle of attack at Mach numbers 1.5 and 2.0. The wing-cone model was tested in the Langley UPWT at Reynolds numbers of 1×10^6 per foot, 2×10^6 per foot, and 4×10^6 per foot. The range of angle of attack was from $-4°$ to $27°$, and the range of sideslip was from $-8°$ to $8°$ for selected angles of attack. The configuration variables investigated included wing longitudinal position, wing incidence angle, vertical-tail arrangement, canard planform, and nose bluntness. Force and moment data were acquired with a six-component strain-gauge balance, and flow visualization characteristics were obtained from schlieren photographs. Test results for this configuration in the Mach 2.5 to 4.5 speed range have been reported in reference 2, and the transonic and subsonic test results are reported in references 3 and 4. This paper presents the experimental study of the configuration at low supersonic Mach numbers. For simplicity, the test model did not have a scramjet engine package.

Symbols

The aerodynamic coefficients are referred to the body-axis system unless otherwise noted. Lift and drag are referred to the stability-axis system. A complete index of data in the body-axis and stability-axis systems is presented in appendix A. The data were reduced about a moment reference center located at 62 percent of the reference fuselage length. This moment reference center was chosen as the quarter-chord point of the theoretical mean aerodynamic chord. (See fig. 1(a).)

b	wingspan, 10.80 in.
b_v	span of vertical tail
C_A	axial-force coefficient, $\frac{\text{Axial force}}{qS}$
$C_{A,c}$	chamber axial-force coefficient, $\frac{\text{Chamber axial force}}{qS}$
C_D	drag coefficient, $\frac{\text{Drag}}{qS}$
$C_{D,c}$	chamber drag coefficient, $\frac{\text{Chamber drag}}{qS}$
$C_{D,o}$	drag coefficient at zero lift
C_L	lift coefficient, $\frac{\text{Lift}}{qS}$
C_l	rolling-moment coefficient, $\frac{\text{Rolling moment}}{qSb}$

$C_{l,s}$	stability-axis rolling-moment coefficient, $\frac{\text{Rolling moment}}{qSb}$
C_{l_β}	lateral-stability derivative, $\frac{(C_l)_{\beta=3^\circ} - (C_l)_{\beta=0^\circ}}{3}$
$\left(C_{l_\beta}\right)_s$	stability-axis lateral-directional stability derivative, $\frac{(C_{l,s})_{\beta=3^\circ} - (C_{l,s})_{\beta=0^\circ}}{3}$
C_m	pitching-moment coefficient, $\frac{\text{Pitching moment}}{qS\overline{c}}$
C_N	normal-force coefficient, $\frac{\text{Normal force}}{qS}$
C_n	yawing-moment coefficient, $\frac{\text{Yawing moment}}{qSb}$
$C_{n,s}$	stability-axis yawing-moment coefficient, $\frac{\text{Yawing moment}}{qSb}$
C_{n_β}	directional-stability derivative, $\frac{(C_n)_{\beta=3^\circ} - (C_n)_{\beta=0^\circ}}{3}$
$\left(C_{n_\beta}\right)_s$	stability-axis directional-stability derivative, $\frac{(C_{n,s})_{\beta=3^\circ} - (C_{n,s})_{\beta=0^\circ}}{3}$
C_{VT}	vertical-tail coefficient
C_Y	side-force coefficient, $\frac{\text{Side force}}{qS}$
C_{Y_β}	side-force derivative, $\frac{(C_Y)_{\beta=3^\circ} - (C_Y)_{\beta=0^\circ}}{3}$
c	wing chord length, in.
$\overline{c}$	mean aerodynamic chord, 14.40 in.
F.S.	fuselage station
L	reference body length, 36.00 in.
L/D	lift-drag ratio
$(L/D)_{\max}$	maximum lift-drag ratio
l_{CG}	location of model moment reference center, 22.32 in.
l_v	distance from vertical-tail MAC to model moment reference center, in.
M	free-stream Mach number
MAC	mean aerodynamic center
P_o	tunnel stagnation pressure, psi
q	free-stream dynamic pressure, psi
R	Reynolds number, per foot
r	nose radius, in.
S	wing reference area, 116.64 in^2
S_v	exposed planform vertical-tail area, in^2
T_o	total tunnel temperature, °F
v	variable
x_{CP}/L	longitudinal location of center of pressure referenced to body length
α	angle of attack, deg
β	angle of sideslip, deg
δ_i	wing incidence, deg

Configuration nomenclature:

B	body
C1	delta canard
C2	trapezoidal canard
N2	nose with $r = 0.050$ in.
N3	nose with $r = 0.124$ in.
N4	nose with $r = 0.010$ in. (used with canards)
N5	nose with $r = 0.002$ in.
V1	large centerline vertical tail
V2	small centerline vertical tail
V3	wing-mounted vertical tails
W	wing in baseline (mid) position at zero incidence
WA	wing in aft position at zero incidence
WF	wing in forward position at zero incidence

Model Description

The test model was basically a conical fuselage fitted with a diamond airfoil delta wing. A sketch of the baseline model along with various component parts is shown in figure 1. The fuselage consisted of a 5° half-angle conical forebody with a circular cylindrical midbody and a 9° truncated conical afterbody. The model had a 4-percent-thick diamond airfoil delta wing of aspect ratio 1, which could be located

at three longitudinal positions and five incidence angles ($-5.0°, -2.5°, 0°, 2.5°$, and $5.0°$). The model components included two canards with different aspect ratios and planforms and four separate noses with radii ranging from 0.002 in. to 0.124 in. The nose with radius $r = 0.010$ in. (N4) was designed to accommodate the canards. Three separate vertical-tail arrangements were tested: a large centerline-mounted tail, a smaller centerline-mounted tail, and twin wing-mounted tails. The vertical-tail volumes were calculated for the three configurations with supersonic flow conditions assumed. The large and small centerline vertical-tail configurations had tail coefficients of 0.209 and 0.115, respectively. The tail volume for the wing-mounted vertical tails was calculated by summing the contributions from both pairs of the wingtip vertical tails, both upper and lower surfaces. It was calculated to be 0.196 in^3, which closely approximates the tail coefficient for the large centerline vertical tail.

Appendix B outlines the method used to compute the vertical-tail coefficient. The baseline configuration consisted of the fuselage with the sharpest nose and the delta wing in the center longitudinal position. Figure 2 shows a photograph of the model installed in the test section. Table I presents a complete description of the geometric characteristics of the model.

Wind Tunnel and Test Conditions

This experimental investigation was conducted in the NASA Langley Unitary Plan Wind Tunnel (UPWT). The UPWT operates in the closed-circuit continuous flow mode over a range of pressure and temperature. The facility has two supersonic test sections, each having dimensions of 4 ft $\times$ 4 ft $\times$ 7 ft. Test section 1 has a Mach number range from 1.5 to 2.9, and test section 2 has a Mach number range from 2.3 to 4.6. Reference 5 presents a complete description of the UPWT along with test section calibration details. For this investigation, the aerodynamic performance of the model was evaluated at Mach 1.5 and 2.0. The nominal test Reynolds number was 2×10^6 per foot; however, selected tests were also conducted at Reynolds numbers of 1×10^6 per foot and 4×10^6 per foot to assess Reynolds number effect. A summary of the test conditions is shown in table II.

The test angle of attack ranged from $-4°$ to $27°$ at sideslip angles of $0°$ and $3°$. Angle of sideslip varied from $-8°$ to $8°$ for selected angles of attack. This was done to establish the linearity of the lateral-directional and side-force coefficients in order to evaluate the reliability of their computed derivatives. For the lower Mach number, the angle-of-attack range was limited to about $15°$ to avoid interference effects due to shock-wave reflections from the test section ceiling. The model angle of incidence was corrected for the effects of sting and balance deflections under aerodynamic loading as well as for tunnel flow misalignment.

Boundary-layer transition on the model was fixed by sprinkling a narrow strip of number 50 sand grit on the model. The grit was applied 0.4 in. aft streamwise from the leading edge of the wing, canard, and vertical tails and 1.2 in. aft of the model nose as measured along the surface. The grit size and location were selected in accordance with the procedures detailed in references 6, 7, and 8 in order to ensure fully turbulent flow over the entire model at low angles of attack. At the higher angles of attack, where fuselage cross-flow separation and wing leading-edge separation can occur, some uncertainty exists as to the extent of the turbulent flow region over the model.

Measurements and Corrections

The aerodynamic forces and moments were measured with a six-component strain-gauge balance housed within the model. The balance was attached to a support sting connected to the permanent model actuating system in the test section. The balance accuracy was estimated at 0.5 percent of the full-scale output of each of the six components.

Balance chamber pressures were measured from tubes placed within the model chamber and adjacent to the support sting. The chamber pressures were used to correct the force data to a condition of free-stream static pressure at the base of the model. The aerodynamic data were reduced about a moment reference center located at 62 percent of the reference body length.

Table III shows the accuracies associated with each of the six body-axis aerodynamic coefficients for the test conditions. The last column in the table shows the error in the chamber axial-force readings based on a pressure transducer accuracy of ± 3 psf.

Results and Discussion

The experimental data are tabulated in microfiche form in tables AIV and AV, which are included in an envelope at the back of the report. The data are plotted in figures 3 through 33. Unless otherwise indicated, the results presented in the following figures are for a Reynolds number of 2×10^6 per foot:

Longitudinal Aerodynamic Characteristics

In general, variations in Reynolds number cause insignificant incremental differences in the longitudinal aerodynamic characteristics. The data showing Reynolds number effects are presented in figures 3, 4, and 5 for the body-alone (BN5), wing-body (WBN5), and large centerline vertical-tail configurations (WBN5V1), respectively. With the exception of the axial force (C_A) and zero-lift drag ($C_{D,o}$) coefficients, the longitudinal aerodynamic coefficients show minimal Reynolds-number-induced incremental differences, especially at angles of attack below 8°. At higher angles, only an insignificant effect is observed. With the exception of the body-alone configuration at Mach 2.0, the axial force and zero-lift drag coefficient values exhibit the expected trend of decreasing value with increasing Reynolds number. The data demonstrate positive nonlinear increments in C_L with increasing angle of attack for all the configurations, irrespective of Reynolds number. References 9 and 10 involve an experimental investigation of the supersonic aerodynamic characteristics of delta wings. These reports present data that demonstrate that with increasing angle of attack, the positive lift increments produced separately by the upper surface (vortex lift) and by the lower surface (compression) are nonlinear. Because of these nonlinear effects, a noticeable break is seen in the lift-curve slope.

Mach number effects are presented in figures 6, 7, 8, and 9 for the body-alone, wing-body, large centerline vertical-tail, and delta canard (WBN4C1) configurations, respectively. The following general trends are observed for increasing Mach number: stability

level decreases (except for BN5), normal-force coefficient curve and lift-curve slope decrease (except for BN5), maximum lift-drag ratio increases, and zero-lift drag and axial-force coefficients decrease. The data also show that for a given lift condition the drag due to lift increases with increasing Mach number.

Figure 10 shows the effects of configuration buildup on the longitudinal aerodynamic characteristics. Comparisons between the body-alone and wing-body configurations indicate that the wing-body configuration exhibits the typical results of reduced drag due to lift and increased lift, L/D, stability level, and zero-lift drag. The wing affects the stability level by shifting the configuration center of pressure aft of the model moment center, which explains the marked contrast in stability levels between the body-alone and wing-body configurations. As expected, the large vertical tail increases zero-lift drag because of the increased skin friction and wave drag. Moreover, it is observed that the addition of the vertical-tail component (WBN5V1) has a slight destabilizing influence. This is possibly due to the positive pitching moment caused by the drag force on the vertical tail, which is located above the model moment reference center. Another possible explanation for the positive increment in pitching-moment coefficient could be the downward force on the vehicle afterbody originating from the shock-induced high-pressure field surrounding the vertical tail. This destabilizing trend is more noticeable at the higher angles of attack.

Figure 11 shows the effects of the vertical-tail arrangements on the longitudinal aerodynamic characteristics. The data show that the wing-mounted vertical tails (V3) exhibit a more stabilizing influence than the other vertical-tail configurations. This characteristic is possibly because the twin tails tend to act like "flow fences" that increase the effectiveness of the wing lower surface. Only the wing-mounted vertical-tail arrangement exhibits at least a minimal effect on the normal-force coefficient and the lift-curve slope, and this is only at the higher angles of attack at Mach 2.0. The wing-mounted vertical tails also incur a slightly higher drag penalty at the zero-lift condition because of the larger tail surface area. The results show that L/D is not significantly affected by vertical-tail arrangement.

The effects of both the delta canard (C1) and the trapezoidal canard (C2) on the aerodynamic characteristics are presented in figure 12. The data show that with the addition of the canards, the stability decreases, the axial-force and normal-force coefficients increase, the lift-curve slope increases, L/D is essentially unchanged, the zero-lift drag coefficient is not affected, and the drag due to lift decreases slightly. Differences in the aerodynamic characteristics produced by the two canards are most likely due to differences in the total wetted surface area, airfoil section geometry, and aspect ratio. For example, the trapezoidal canard configuration (WBN5C2) shows a more positive pitching moment than the delta canard configuration (WBN5C1), possibly due in part to a slightly higher lift coefficient caused by a larger aspect ratio. More importantly, the center of pressure for the trapezoidal canard configuration is farther forward than for the delta canard configuration, which results in a larger moment arm and a higher pitching-moment coefficient. Furthermore, the relative difference in pitching-moment coefficient between the two canards for $C_L < 0.30$ is not consistent between Mach numbers. This is because the delta canard produces a larger forward shift in the center of pressure at the higher Mach numbers. At Mach 2.0, the centers of pressure for both canard types are located at nearly equal longitudinal positions, resulting in nearly identical moment arms for the two canard planforms. This phenomenon reduces the relative difference in pitching-moment coefficient between the two canard configurations at Mach 2.0. Both configurations begin to exhibit neutral stability around angles of attack of 16° and 20° for the trapezoidal and delta canard configurations, respectively. However, both configurations resume their stable trends around an angle of attack of 23°.

Figure 13 shows the effects of wing longitudinal position on the aerodynamic characteristics. The data typically show that the aerodynamic trends vary successively from one extreme to another as the wing is moved from the forward to the aft position. Generally, moving the wing to the forward position (WFBN5) results in decreased stability level, increased axial- and normal-force coefficients, increased lift-curve slope, and no appreciable change in zero-lift drag or lift-drag ratio. The induced drag characteristics at the lower Mach number are nearly identical to those of the configuration with the wing in the midposition. At the higher Mach number, however, the forward-positioned wing appears to show more favorable induced drag characteristics. However, the significance of this trend is questionable, since the apparent drag decrement achieved with the WFBN5 configuration is roughly on the order of the strain-gauge balance accuracy under the specified test conditions. Moving the wing to the aft position (WABN5) results in an increased stability margin, decreased axial- and normal-force coefficients, decreased lift-curve slope, and no significant change in the zero-lift drag. The induced drag

characteristics appear to be more desirable at the lower Mach number, but again, these results are questionable based on consideration of the balance accuracy. A barely noticeable increase in $(L/D)_{max}$ at Mach 1.5 is produced when the wing is in the rearmost position. The effect of wing position on $(L/D)_{max}$ at Mach 2.0 is not significant. The differences in aerodynamic characteristics as a function of wing longitudinal position are probably due to wing-body interference effects and to the different center of pressure locations relative to the model reference center. A closer examination of the data reveals that at Mach 1.5, the distance that the wing is shifted (1.80 in.) corresponds roughly to the distance traveled by the center of pressure. At Mach 2.0, the correspondence is not as closely coupled. This disparity could be because the location of the configuration center of pressure is not as strongly dictated by wing longitudinal position at Mach 2.0 as it is at Mach 1.5 and because the influence upon total lift by the body increases with Mach number. This hypothesis is supported by the data shown in figures 6 and 7, which reveal that the lift-curve slope for the body-alone case increases with Mach number but that the opposite trend is observed for the wing-body case.

Data were taken when the wing was set at selected positive or negative incidence angles with respect to the fuselage. The rationale behind setting the wings at positive incidence angles is based on the fact that adequate lift can be obtained even when the fuselage is at angles of attack near 0°. This orientation would maximize the flow-field quality at the inlet of an engine designed to be wrapped circumferentially around the cylindrical midsection of the vehicle. Test results by Wood and Miller (ref. 11) suggest that favorable lift characteristics can be obtained for positive fuselage incidence angles because of fuselage-induced upwash, which increases the effective local angle of attack near the wing. In figure 14 the effects of wing incidence on the aerodynamic characteristics are shown. The data were examined for the case with the model angle of attack set equal to the negative of the wing incidence angle and with the delta wings aligned with the free-stream flow. Comparisons with the body-alone data shown in figure 10 indicate that the amount of positive or negative lift obtained from the wing-body configuration with wing incidence slightly exceeds the amount of lift obtained with just the body alone at comparable pitch angles. This result is consistent with slender-body theory, which incorporates wing-body interference effects such as forebody-induced upwash. Generally, the increments in pitching moment for the various angles of incidence are fairly constant across the tested angle-of-attack range. The normal-force coefficient increments are likewise fairly constant, while the axial force increases with increasing angle of wing incidence. Only marginal differences are found with variation of wing incidence for the zero-lift drag, drag due to lift, and the lift-drag ratio.

The effects of nose bluntness on the longitudinal characteristics are presented in figure 15. The data are shown for the sharpest, moderately blunt, and most blunt noses (N5, N2, and N3, respectively). The results show that the aerodynamic characteristics are generally insensitive to nose bluntness. However, the data show that the sharp nose (N5) configuration does produce a noticeable increment in lift at Mach 2.0 at high angles of attack.

Lateral-Directional Aerodynamic Characteristics

One of the most dominant aerodynamic phenomena associated especially with lateral-directional stability is the interaction between asymmetric vortices and various model components. These asymmetric vortices arise from cross-flow separation of the forebody boundary layers, which contain vorticity produced by the velocity gradient near the model surface. References 12, 13, and 14 treat the subject of vortex shedding with respect to interference effects. Shown in figure 16 are the lateral-directional and side-force data as a function of configuration buildup at a sideslip angle of 0°. The data show neutral lateral-directional and side-force coefficients for angles of attack less than 12°. For higher angles, the coefficients show significant nonlinearities at Mach 2.0. These effects are due to the interaction of the model components with the free forebody vortices. Figure 17 presents the effects of the vertical-tail arrangement on the lateral-directional and side-force data at a sideslip angle of 0°. As shown previously, the data reveal marked nonlinearities at Mach 2.0 for the higher angles of attack. The configuration with the large centerline vertical tail displays the greatest magnitude of nonlinearity. According to reference 12, some of the factors that affect the angle of attack for the onset of vortex asymmetries include nose bluntness, strakes, nose half-angle, Mach number, and Reynolds number. For example, it has been found that for models with pointed noses, the onset of vortex asymmetries occurs at an angle of attack approximately equal to twice the semiapex angle. This characteristic was observed in previous tests of the same vehicle at higher supersonic and transonic Mach numbers (refs. 2 and 3).

In order to determine the linearity of the lateral-directional characteristics, data were acquired on

various configurations for β sweeps over $\pm 8°$ at selected angles of attack. The data from these runs are presented in figures 18 through 24 and show that all test configurations have almost linear lateral-directional characteristics over a sideslip range of $\pm 3°$ up to the maximum tested angles of attack of 15° at Mach 1.5 and 20° at Mach 2.0. Thus α-sweep tests were conducted on configurations of interest at constant sideslip angles of 0° and 3° to establish the lateral-directional stability derivatives. It must be noted that the data for the stability derivatives were obtained over a wider range of angle of attack than was used to establish linearity and that the stability derivatives at the higher angles of attack must be used with caution. For example, at an angle of attack of 20° the data in several cases show nonlinearities. This effect is due to the aforementioned interaction between the shed forebody vortices and the various model components. Since the onset angle for this interaction occurs at an angle of attack of about 12°, critical judgement must be exercised in evaluating the reliability of stability derivatives calculated at the higher angles.

Figures 25 to 33 show the lateral-directional stability and side-force derivatives obtained from the α sweeps at sideslip angles of 0° and 3°. The Mach number effects are shown in figures 25 to 28 for the body-alone, baseline wing-body, wing-body large centerline vertical tail, and wing-body delta canard configurations. Configuration WBN5V1 is stable at both Mach numbers below angles of attack of 20°, but demonstrates the expected trend of decreasing stability with increasing Mach number. This phenomenon is attributed to the fact that the lift-curve slope of the vertical tail decreases with increasing Mach number, whereas the forces and moments affecting the fuselage remain basically constant (ref. 15).

The comparative effects of the vertical-tail configurations are shown in figure 29. The large centerline vertical tail produces the most directionally stable configuration. The data also show that for the centerline vertical tails, the directional stability and side-force derivatives deteriorate with increasing angle of attack. Conversely, the wing-mounted vertical-tail configuration demonstrates improved lateral-directional characteristics at higher angles of attack. The centerline vertical tails lose effectiveness at the higher angles of attack because of fuselage shielding and wake flow from the wing. With the outboard wing-mounted vertical tails, neither fuselage shielding nor wake interference has as much of an effect as observed with the centerline vertical tails.

Figure 30 shows the effect of the canards on the lateral-directional stability and side-force derivatives. The test results show that the delta canard configuration (WBN4C1) is more directionally stable than the trapezoidal canard configuration (WBN4C2) as angle of attack increased. Both configurations exhibit positive lateral stability for positive angles of attack, but the delta canard shows slightly higher stability for angles of attack below 16°. The side-force characteristics are stable across the tested range of angle of attack for both canards, but generally the trapezoidal canard (C2) shows greater stability with increasing angle of attack.

Figures 31 and 32 present the effects of wing position and wing incidence on the lateral-directional characteristics. The effect of wing longitudinal position on the directional stability is minimal, but the roll characteristics improve as the wing is translated forward. The data also show that the side-force derivative is most favorable when the wing is in the aft position. For the variation in wing incidence angles, the data show that improved directional stability and side-force characteristics are achieved with increasingly negative wing incidence angles. Conversely, positive wing incidence angles, generally, enhance the lateral stability derivative. The data at the higher Mach number show erratic tendencies that are probably due to interactions between asymmetric forebody vortices and the model components.

Figure 33 shows the effect of nose bluntness on the lateral-directional and side-force characteristics. Data were acquired for the baseline wing-body configuration with the sharp nose (WBN5), the wing-body with the moderately blunt nose (WBN2), and the wing-body with the bluntest nose (WBN3). The sharp nose configuration appears to show slightly improved directional stability at the high angles of attack at Mach 2.0. The lateral stability appears to be unaffected by nose bluntness. Finally, the side-force stability derivative for the sharp nose configuration shows less favorable characteristics than both the moderately blunt and the extremely blunt noses at angles of attack greater than 12°. However, these trends will have to be evaluated, given the fact that unsteady aerodynamic characteristics occur at the higher angles of attack because of asymmetric effects.

Concluding Remarks

An experimental investigation was conducted to evaluate the longitudinal and lateral-directional stability characteristics of a wing-cone model at Mach 1.5 and 2.0. The nominal test Reynolds number was 2×10^6 per foot, but selected data were also

acquired at Reynolds numbers of 1×10^6 per foot and 4×10^6 per foot. Data were acquired for an angle-of-attack range from $-4°$ to $27°$ at sideslip angles of $0°$ and $3°$ and for an angle-of-sideslip range from $-8°$ to $8°$ at selected angles of attack. Model variations included wing longitudinal position and incidence, canard planform, vertical-tail arrangement, wing incidence angle, and nose bluntness.

The Reynolds number effects were as expected. The longitudinal stability decreased with increasing Mach number, as did the normal-force coefficient and the lift-curve slope.

As expected, the lift-curve slope of the wing-body configuration (WBN5) decreased with increasing Mach number, unlike the body-alone configuration, which exhibited the opposite trend with increasing Mach number. This result could indicate that as Mach number increases, the contribution to the total lift from the body also increases.

The wing-mounted vertical tails resulted in the greatest longitudinal stability margin. The following aerodynamic characteristics were not significantly affected by vertical-tail arrangement: normal force, lift-curve slope, zero-lift drag, drag due to lift, and maximum lift-drag ratio.

As expected, the canards increased the lift-curve slope, made the vehicle more longitudinally unstable, and noticeably improved the drag-due-to-lift performance. When referenced to the baseline configuration, the trapezoidal canard resulted in a larger increase in pitching moment than the delta canard. At Mach 2.0, the pitching-moment levels were nearly the same for the two canard configurations up to an angle of attack of about $12°$. However, above this angle, the trapezoidal canard configuration produced a higher pitching moment than the delta canard. Additionally, both configurations began to exhibit neutral stability for a limited angle-of -attack range above which both configurations resumed their stable trends.

When the wing was in the forward position, the lift-curve slope increased and the longitudinal stability decreased. The opposite effects were obtained when the wing was in the rearmost position.

The increments in pitching-moment, normal-force, and lift coefficients were fairly constant for variations in wing incidence, but the differences in zero-lift drag, drag due to lift, and lift-drag ratio were negligible. However, the data showed that the maximum lift-drag ratio was achieved for a wing incidence of $-2.5°$ at Mach 2.0.

Although the most favorable lateral-directional characteristics were achieved with the large centerline vertical tail, the effectiveness of this configuration decreased with increasing angle of attack and Mach number. The wing-mounted vertical tails did not lose their effectiveness as much as the centerline vertical tails with increasing Mach number or angle of attack.

The delta canard produced lateral-directional characteristics that were slightly better than those for the trapezoidal canard.

At the high angles of attack, the lateral-directional data showed asymmetric behavior, possibly due to unbalanced aerodynamic loads arising from interactions between the vehicle components and asymmetric vortices shed from the forebody.

NASA Langley Research Center
Hampton, VA 23681-0001
December 10, 1992

References

1. Escher, William J. D.: Synerjet: Beyond the Shuttle. *Spaceflight,* vol. 14, no. 11, Nov. 1972, pp. 413–416.

2. Covell, Peter F.; Walker, Ira J.; and Howell, Dorothy T.: *Longitudinal and Lateral-Directional Aerodynamic Characteristics of a Wing-Cone Configuration at Mach Numbers From 2.5 to 4.5.* NASA TM-4337, 1992.

3. Luckring, James M.; Fox, Charles H., Jr.; and Cundiff, Jeffrey S.: Reynolds Number Effects on the Transonic Aerodynamics of a Slender Wing-Body Configuration. *Transonic Symposium: Theory, Application, and Experiment,* Jerome T. Foughner, Jr., compiler, NASA CP-3020, Vol. II, 1989, pp. 41–58.

4. Gatlin, Gregory M.: *Low-Speed, High-Lift Aerodynamic Characteristics of Slender, Hypersonic Accelerator-Type Configurations.* NASA TP-2945, 1989.

5. Jackson, Charlie M., Jr.; Corlett, William A.; and Monta, William J.: *Description and Calibration of the Langley Unitary Plan Wind Tunnel.* NASA TP-1905, 1981.

6. Braslow, Albert L.; Hicks, Raymond M.; and Harris, Roy V., Jr.: *Use of Grit-Type Boundary-Layer-Transition Trips on Wind-Tunnel Models.* NASA TN D-3579, 1966.

7. Stallings, Robert L., Jr.; and Lamb, Milton: *Effects of Roughness Size on the Position of Boundary-Layer Transition and on the Aerodynamic Characteristics of a 55° Swept Delta Wing at Supersonic Speeds.* NASA TP-1027, 1977.

8. Wassum, Donald L.; and Hyman, Curtis E., Jr.: *Procedures and Requirements for Testing in the Langley Research Center Unitary Plan Wind Tunnel.* NASA TM-100529, 1988.

9. Wood, Richard M.; and Miller, David S.: Assessment of Preliminary Prediction Techniques for Wing Leading-Edge Vortex Flows at Supersonic Speeds. AIAA-84-2208, Aug. 1984.

10. Wood, Richard M.: *Supersonic Aerodynamics of Delta Wings.* NASA TP-2771, 1988.

11. Wood, Richard M.; and Miller, David S.: *Effect of Fuselage Upwash on the Supersonic Longitudinal Aerodynamic Characteristics of Two Fighter Configurations.* NASA TP-2330, 1984.

12. Nielsen, Jack N.: Nonlinearities in Missile Aerodynamics. AIAA Paper 78-20, Jan. 1978.

13. Thomson, K. D.; and Morrison, D. F.: The Spacing, Position and Strength of Vortices in the Wake of Slender Cylindrical Bodies at Large Incidence. *J. Fluid Mech.,* vol. 50, pt. 4, Dec. 29, 1971, pp. 751–783.

14. Chapman, Gary T.; Keener, Earl R.; and Malcolm, Gerald N.: Asymmetric Aerodynamic Forces on Aircraft Forebodies at High Angles of Attack—Some Design Guides. *Stall/Spin Problems of Military Aircraft,* AGARD-CP-199, June 1976, pp. 12-1–12-9.

15. Spearman, M. Leroy: *Some Factors Affecting the Static Longitudinal and Directional Stability Characteristics of Supersonic Aircraft Configurations.* NACA RM L57E24a, 1957.

Table I. Geometric Characteristics of the Model

Wing W1:	
Theoretical area (reference), in^2	11 6.64
Aspect ratio	1. 00
Span, in.	10. 80
Leading-edge sweep, deg	75.96
Trailing-edge sweep, deg	0.00
Mean aerodynamic chord, in.	14.40
Airfoil section	Diamond
Airfoil thickness-to-chord ratio, percent	4.0
Vertical tail V1, body centerline:	
Exposed area, in^2	20.92
Span, in.	5.846
Leading-edge sweep, deg	70.0
Trailing-edge sweep, deg	38.13
Airfoil section	Diamond
Airfoil thickness-to-chord ratio (parallel to 9° boattail), percent	4.0
Vertical-tail coefficient	0.209
Vertical tail V2, body centerline:	
Exposed area, in^2	12.91
Span, in.	4.435
Leading-edge sweep, deg	70.0
Trailing-edge sweep, deg	−1.96
Airfoil section	Diamond
Airfoil thickness-to-chord ratio (parallel to 9° boattail), percent	4.0
Vertical-tail volume, in^3	0.115
Vertical tail V3, wing mounted:	
Upper surface vertical:	
Exposed area, in^2	6.46
Span, in.	2.320
Leading-edge sweep, deg	70.0
Trailing-edge sweep, deg	55.0
Airfoil section	Diamond
Airfoil thickness-to-chord ratio, percent	4.0
Vertical-tail coefficient	0.055
Lower surface vertical:	
Exposed area, in^2	5.19
Span, in.	1.800
Trailing-edge sweep, deg	55.0
Airfoil section	Diamond
Airfoil thickness-to-chord ratio, percent	4.0
Vertical-tail coefficient	0.043

Table I. Concluded

Canard C1 (delta):	
Exposed area, in^2	5.99
Theoretical aspect ratio	1. 87
Span, in.	4.50
Leading-edge sweep, deg	65.0
Trailing-edge sweep, deg	0.0
Airfoil section	Diamond
Airfoil thickness-to-chord ratio, percent	6.0
Incidence angle, deg	0.0
Canard C2 (trapezoidal):	
Exposed area, in^2	5.00
Theoretical aspect ratio	5.48
Span, in.	6.05
Leading-edge sweep, deg	16.0
Trailing-edge sweep, deg	0.0
Airfoil section	NACA 0006
Incidence angle, deg	0.0
Axisymmetric fuselage B:	
Theoretical length, in.	36.00
Cone half-angle, deg	5.0
Cylinder radius (maximum), in.	2.317
Boattail half-angle, deg	9.0
Base (chamber) area, in^2	4.352
Moment reference center, in.	22.32
Radius of sharp nose (N5), in.	0.005
Radius of canard nose (N4), in.	0.012
Radius of blunt nose (N3), in.	0.124

Table II. Summary of Test Conditions

M	P_o, psi	q, psi	T_o, °F	R
1.5	3.65	1.57	125	1×10^6
2.0	4.35	1.56	125	1
1.5	7.30	3.13	125	2
2.0	8.70	3.11	125	2
1.5	14.60	6.26	125	4
2.0	17.41	6.23	125	4

Table III. Coefficient Accuracy

			Maximum absolute error for—						
M	R	q, psi	C_N	C_A	C_m	C_l	C_n	C_Y	$C_{A,c}$
1.5	1×10^6	1.57	0.0082	0.0016	0.0019	0.0003	0.0010	0.0055	0.0005
2.0	1	1.56	.0083	.0017	.0019	.0003	.0010	.0055	.0005
1.5	2	3.13	.0041	.0008	.0010	.0001	.0005	.0027	.0002
2.0	2	3.11	.0041	.0008	.0010	.0001	.0005	.0028	.0002
1.5	4	6.26	.0021	.0004	.0005	.0001	.0003	.0014	.0001
2.0	4	6.23	.0021	.0004	.0005	.0001	.0003	.0014	.0001

Appendix A

Tabulated Data

Table AI defines the symbols corresponding to the column headings of the tabulated force and moment data and the tabulated lateral-directional stability derivatives. Table AII is an index to the tabulated force and moment data, which are presented in the microfiche supplement as table AIV. Table AIII is an index to the tabulated lateral-directional stability derivatives, which are presented in the microfiche supplement as table AV.

Table AI. Symbols for Tabulated Data

Tabulated data heading	Definition
ALPHA	α
BETA	β
CA	C_A
CAC	$C_{A,c}$
CA UNC	C_A (uncorrected)
CD	C_D
CDC	$C_{D,c}$
CD UNC	C_D (uncorrected)
CL	C_L
CLB	C_l
CLBB	C_{l_β}
CLS	$C_{l,s}$
CLSB	$\left(C_{l_\beta}\right)_s$
CLSQ	C_L^2
CM	C_m
CN	C_N
CNB	C_n
CNBB	C_{n_β}
CNS	$C_{n,s}$
CNSB	$\left(C_{n_\beta}\right)_s$
CY	C_Y
CYBB	C_{Y_β}
L/D	L/D
MACH	M
R/FT	$R \times 10^{-6}$
RUN	Run number
RUNB0	(Run number) $_{\beta=0^o}$
RUNB3	(Run number) $_{\beta=3^o}$
XCP/L	x_{CP}/L

Table AII. Index to Tabulated Force and Moment Data

Configuration	R	α, deg	β, deg	Run number for M =	
				1.5	2.0
WBN5	1×10^6	v	0	5	27
↓	1	v	0	6	28
	1	v	0	7	29
	1	v	3	8	30
	1	0	v	9	31
	1	5	v	10	32
	1	10	v	11	33
	1	20	v		34
	2	v	0	13	35
	2	v	0	14	36
	2	v	0	15	43
	2	v	3	16	44
	2	0	v	17	39
	2	5	v	18	40
	2	10	v	19	41
	2	20	v		42
	4	v	0	20	47
	4	v	0	21	46
	4	v	0	22	48
	4	v	3	23	49
	4	0	v	24	50
	4	5	v	25	51
	4	10	v	26	52
WBN5V1	1×10^6	v	0	61	91
↓	1	v	3	62	92
	1	0	v	63	93
	1	5	v	64	94
	1	10	v	65	95
	1	20	v	66	96
	2	v	0	67	85
	2	v	3	68	86
	2	0	v	69	87
	2	5	v	70	88
	2	10	v	71	89
	2	20	v	72	90
	4	v	0	73	79
	4	v	3	74	80
	4	0	v	75	81
	4	5	v	76	82
	4	10	v	77	83
↓	4	20	v	78	84
WBN5V2	2×10^6	v	0	97	103
↓	2	v	3	98	104
	2	0	v	99	105
	2	5	v	100	106
	2	10	v	101	107
↓	2	20	v	102	108

Table AII. Continued

Configuration	R	α, deg	β, deg	Run number for $M =$	
				1.5	2.0
WBN5V3	2×10^6	v	0	109	115
↓	2	v	3	110	116
	2	0	v	111	117
	2	5	v	112	118
	2	10	v	113	119
	2	20	v	114	120
WBN4C1	2×10^6	v	0	121	127
↓	2	v	3	122	128
	2	0	v	123	129
	2	5	v	124	130
	2	10	v	125	131
	2	20	v	126	132
WBN4C2	2×10^6	v	0	133	139
↓	2	v	3	134	140
	2	0	v	135	141
	2	5	v	136	142
	2	10	v	137	143
	2	20	v	138	144
WFBN5	2×10^6	v	0	145	151
↓	2	v	3	146	152
	2	0	v	147	153
	2	5	v	148	154
	2	10	v	149	155
	2	20	v	150	156
WABN5	2×10^6	v	0	157	163
↓	2	v	3	158	164
	2	0	v	159	165
	2	5	v	160	166
	2	10	v	161	167
	2	20	v	162	168
WBN5, $\delta_i = 5°$	2×10^6	v	0	169	180
↓	2	v	3	170	181
	2	0	v	171	182
	2	5	v	172	183
	2	10	v	173	184
	2	20	v	174	185
WBN5, $\delta_i = -5°$	2×10^6	v	0	175	186
↓	2	v	-3	176	187
	2	-5	v	177	188
	2	-10	v	178	189
	2	-20	v	179	190

Table AII. Concluded

Configuration	R	α, deg	β, deg	Run number for M =	
				1.5	2.0
WBN5, $\delta_i = 2.5°$	2×10^6	v	0	191	202
↓	2	v	3	192	203
	2	0	v	193	204
	2	5	v	194	205
	2	10	v	195	206
	2	20	v	196	207
WBN5, $\delta_i = -2.5°$	2×10^6	v	0	197	208
↓	2	v	-3	198	209
	2	-5	v	199	210
	2	-10	v	200	211
	2	-20	v	201	212
WBN3	2×10^6	v	0	213	219
↓	2	v	3	214	220
	2	0	v	215	221
	2	5	v	216	222
	2	10	v	217	223
	2	20	v	218	224
WBN2	2×10^6	v	0	225	231
↓	2	v	3	226	232
	2	0	v	227	233
	2	5	v	228	234
	2	10	v	229	235
	2	20	v	230	236
WBN2V1	2×10^6	v	0	237	243
↓	2	v	3	238	244
	2	0	v	239	245
	2	5	v	240	246
	2	10	v	241	247
	2	20	v	242	248
WBN4C1V1	2×10^6	v	0	249	255
↓	2	v	3	250	256
	2	0	v	251	257
	2	5	v	252	258
	2	10	v	253	259
	2	20	v	254	260
BN5	1×10^6	v	0	261	271
↓	1	v	3	262	272
	2	v	0	263	273
	2	v	3	264	274
	2	0	v	265	275
	2	5	v	266	276
	2	10	v	267	277
	2	20	v	268	278
	4	v	0	269	279
	4	v	3	270	280

Table AIII. Index to Tabulated Lateral-Directional Stability Derivatives

Configuration	R	Run number ($\beta = 0°/\beta = 3°$) for $M =$	
		1.5	2.0
WBN5	1×10^6	7/8	29/30
WBN5	2	15/16	43/44
WBN5	4	22/23	48/49
WBN5V1	1	61/62	91/92
WBN5V1	2	67/68	85/86
WBN5V1	4	73/74	79/80
WBN5V2	2	97/98	103/104
WBN5V3	2	109/110	115/116
WBN4C1	2	121/122	127/128
WBN4C2	2	133/134	139/140
WFBN5	2	145/146	151/152
WABN5	2	157/158	163/164
WBN5, $\delta_i = 5°$	2	169/170	180/181
WBN5, $\delta_i = -5°$	2	175/176	186/187
WBN5, $\delta_i = 2.5°$	2	191/192	202/203
WBN5, $\delta_i = -2.5°$	2	197/198	208/209
WBN3	2	213/214	219/220
WBN2	2	225/226	231/232
WBN2V1	2	237/238	243/244
WBN4C1V1	2	249/250	255/256
BN5	1	261/262	271/272
BN5	2	263/264	273/274
BN5	4	269/270	279/280

Appendix B

Vertical-Tail Coefficient Calculations

The vertical-tail coefficients were calculated for the different vertical-tail arrangements in order to approximate their comparative stabilizing effectiveness. The calculations that follow are based on the aerodynamic characteristics of control surfaces at supersonic speeds. Figure B1 is a diagram of the geometric parameters used to compute the vertical-tail volume.

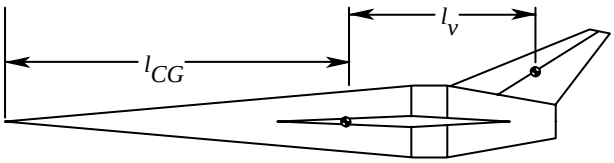

Figure B1. Model dimensions used to compute vertical-tail volume.

The vertical-tail coefficient is calculated by the following equation:

$$C_{VT} = \frac{l_v S_v}{b S} \tag{B1}$$

The parameter l_v is the distance between the mean aerodynamic center (MAC) of the vertical tail and the moment reference center of the model. The parameter S_v is the exposed planform area of the vertical tail. The location of the MAC was estimated as the midchord point of the mean aerodynamic chord of the exposed tail planform. The mean aerodynamic chord was computed using the following integral evaluated in the reference frame of the vertical tail (see fig. B2):

$$\overline{c} = \frac{1}{S_v} \int_0^{b_v} c^2 \, dy \tag{B2}$$

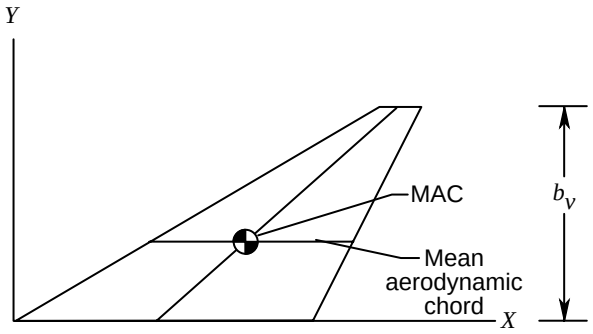

Figure B2. Reference frame for vertical tail.

The total vertical-tail coefficient for the wing-mounted arrangement is computed by combining the tail coefficients for both upper and lower panels as follows:

$$C_{VT,\text{total}} = 2C_{VT,\text{upper}} + 2C_{VT,\text{lower}} \tag{B3}$$

(a) General arrangement of the model. Wing in baseline (mid) position at zero incidence.

Figure 1. Geometric description of wind-tunnel model. All dimensions are given in inches.

(b) Details of noses.

Figure 1. Continued.

(c) Canard details.

(d) Details of centerline-mounted vertical tail.

Figure 1. Continued.

(e) Details of wing-mounted vertical tail.

(f) Wing incidence and location variables.

Figure 1. Concluded.

L-88-6240

Figure 2. Photograph of model mounted in test section 1 of Unitary Plan Wind Tunnel; WBN5V1 configuration.

(a) $M = 1.5$.

Figure 3. Effect of Reynolds number on longitudinal aerodynamic characteristics; BN5.

(b) $M = 1.5$.

Figure 3. Continued.

(c) $M = 1.5$.

Figure 3. Continued.

(d) $M = 2.0$.

Figure 3. Continued.

(e) $M = 2.0$.

Figure 3. Continued.

(f) $M = 2.0$.

Figure 3. Concluded.

(a) $M = 1.5$.

Figure 4. Effect of Reynolds number on longitudinal aerodynamic characteristics; WBN5.

(b) $M = 1.5$.

Figure 4. Continued.

(c) $M = 1.5$.

Figure 4. Continued.

(d) $M = 2.0$.

Figure 4. Continued.

(e) $M = 2.0$.

Figure 4. Continued.

(f) $M = 2.0$.

Figure 4. Concluded.

(a) $M = 1.5$.

Figure 5. Effect of Reynolds number on longitudinal aerodynamic characteristics; WBN5V1.

(b) $M = 1.5$.

Figure 5. Continued.

(c) $M = 1.5$.

Figure 5. Continued.

(d) $M = 2.0$.

Figure 5. Continued.

(e) $M = 2.0$.

Figure 5. Continued.

(f) $M = 2.0$.

Figure 5. Concluded.

Figure 6. Effect of Mach number on longitudinal aerodynamic characteristics; BN5.

Figure 6. Continued.

Figure 6. Concluded.

Figure 7. Effect of Mach number on longitudinal aerodynamic characteristics; WBN5.

Figure 7. Continued.

Figure 7. Concluded.

Figure 8. Effect of Mach number on longitudinal aerodynamic characteristics; WBN5V1.

Figure 8. Continued.

Figure 8. Concluded.

Figure 9. Effect of Mach number on longitudinal aerodynamic characteristics; WBN4C1.

Figure 9. Continued.

Figure 9. Concluded.

(a) $M = 1.5$.

Figure 10. Effect of configuration buildup on longitudinal aerodynamic characteristics; BN5 , WBN5, WBN5V1.

(b) $M = 1.5$.

Figure 10. Continued.

(c) $M = 1.5$.

Figure 10. Continued.

(d) $M = 2.0$.

Figure 10. Continued.

(e) $M = 2.0$.

Figure 10. Continued.

(f) $M = 2.0$.

Figure 10. Concluded.

(a) $M = 1.5$.

Figure 11. Effect of vertical tail on longitudinal aerodynamic characteristics; WBN5.

(b) $M = 1.5$.

Figure 11. Continued.

(c) $M = 1.5$.

Figure 11. Continued.

(d) $M = 2.0$.

Figure 11. Continued.

(e) $M = 2.0$.

Figure 11. Continued.

(f) $M = 2.0$.

Figure 11. Concluded.

(a) $M = 1.5$.

Figure 12. Effect of canard on longitudinal aerodynamic characteristics; WBN5 for canard off, WBN4 for canard on.

(b) $M = 1.5$.

Figure 12. Continued.

(c) $M = 1.5$.

Figure 12. Continued.

(d) $M = 2.0$.

Figure 12. Continued.

(e) $M = 2.0$.

Figure 12. Continued.

(f) $M = 2.0$.

Figure 12. Concluded.

(a) $M = 1.5$.

Figure 13. Effect of wing position on longitudinal aerodynamic characteristics; WBN5.

(b) $M = 1.5$.

Figure 13. Continued.

(c) $M = 1.5$.

Figure 13. Continued.

(d) $M = 2.0$.

Figure 13. Continued.

(e) $M = 2.0$.

Figure 13. Continued.

(f) $M = 2.0$.

Figure 13. Concluded.

(a) $M = 1.5$.

Figure 14. Effect of wing incidence on longitudinal aerodynamic characteristics; WBN5.

(b) $M = 1.5$.

Figure 14. Continued.

(c) $M = 1.5$.

Figure 14. Continued.

(d) $M = 2.0$.

Figure 14. Continued.

(e) $M = 2.0$.

Figure 14. Continued.

(f) $M = 2.0$.

Figure 14. Concluded.

(a) $M = 1.5$.

Figure 15. Effect of nose bluntness on longitudinal aerodynamic characteristics; WBN5, WBN2, WBN3.

(b) $M = 1.5$.

Figure 15. Continued.

(c) $M = 1.5$.

Figure 15. Continued.

(d) $M = 2.0$.

Figure 15. Continued.

(e) $M = 2.0$.

Figure 15. Continued.

(f) $M = 2.0$.

Figure 15. Concluded.

(a) $M = 1.5$.

Figure 16. Asymmetric effects for configuration buildup at $\beta = 0°$; BN5, WBN5, WBN5V1.

(b) $M = 2.0$.

Figure 16. Concluded.

(a) $M = 1.5$.

Figure 17. Asymmetric effects for various vertical-tail arrangements at $\beta = 0°$; WBN5.

(b) $M = 2.0$.

Figure 17. Concluded.

(a) $M = 1.5$.

Figure 18. Effect of angle of attack on lateral-directional aerodynamic characteristics; BN5.

(b) $M = 2.0$.

Figure 18. Concluded.

(a) $M = 1.5$.

Figure 19. Effect of angle of attack on lateral-directional aerodynamic characteristics; WBN5.

(b) $M = 2.0$.

Figure 19. Concluded.

(a) $M = 1.5$.

Figure 20. Effect of angle of attack on lateral-directional aerodynamic characteristics; WBN5V1.

(b) $M = 2.0$.

Figure 20. Concluded.

(a) $M = 1.5$.

Figure 21. Effect of angle of attack on lateral-directional aerodynamic characteristics; WBN5V2.

(b) $M = 2.0$.

Figure 21. Concluded.

(a) $M = 1.5$.

Figure 22. Effect of angle of attack on lateral-directional aerodynamic characteristics; WBN5V3.

(b) $M = 2.0$.

Figure 22. Concluded.

(a) $M = 1.5$.

Figure 23. Effect of angle of attack on lateral-directional aerodynamic characteristics; WBN4C1.

(b) $M = 2.0$.

Figure 23. Concluded.

(a) $M = 1.5$.

Figure 24. Effect of angle of attack on lateral-directional aerodynamic characteristics; WBN4C2.

(b) $M = 2.0$.

Figure 24. Concluded.

Figure 25. Effect of Mach number on lateral-directional stability derivatives; BN5.

Figure 26. Effect of Mach number on lateral-directional stability derivatives; WBN5.

Figure 27. Effect of Mach number on lateral-directional stability derivatives; WBN5 V1.

Figure 28. Effect of Mach number on lateral-directional stability derivatives; WBN4C1.

(a) $M = 1.5$.

Figure 29. Effect of vertical tail on lateral-directional stability derivatives; WBN5.

(b) $M = 2.0$.

Figure 29. Concluded.

(a) $M = 1.5$.

Figure 30. Effect of canard on lateral-directional stability derivatives; WBN5 for canard off, WBN4 for canard on.

(b) $M = 2.0$.

Figure 30. Concluded.

(a) $M = 1.5$.

Figure 31. Effect of wing position on lateral-directional stability derivatives; WBN5.

(b) $M = 2.0$.

Figure 31. Concluded.

(a) $M = 1.5$.

Figure 32. Effect of wing incidence on lateral-directional stability derivatives; WBN5.

(b) $M = 2.0$.

Figure 32. Concluded.

(a) $M = 1.5$.

Figure 33. Effect of nose bluntness on lateral-directional stability derivatives; WBN5, WBN2, WBN3.

(b) $M = 2.0$.

Figure 33. Concluded.

REPORT DOCUMENTATION PAGE

Form Approved
OMB No. 0704-0188

1. AGENCY USE ONLY *(Leave blank)*	2. REPORT DATE	3. REPORT TYPE AND DATES COVERED
	February 1993	Technical Memorandum

4. TITLE AND SUBTITLE
Experimental Aerodynamic Characteristics of a Generic Hypersonic Accelerator Configuration at Mach Numbers 1.5 and 2.0

5. FUNDING NUMBERS
WU 505-59-40-10

6. AUTHOR(S)
Ira J. Walker, Peter F. Covell, and Dana K. Forrest

7. PERFORMING ORGANIZATION NAME(S) AND ADDRESS(ES)
NASA Langley Research Center
Hampton, VA 23681-0001

8. PERFORMING ORGANIZATION REPORT NUMBER
L-17105

9. SPONSORING/MONITORING AGENCY NAME(S) AND ADDRESS(ES)
National Aeronautics and Space Administration
Washington, DC 20546-0001

10. SPONSORING/MONITORING AGENCY REPORT NUMBER
NASA TM-4413

11. SUPPLEMENTARY NOTES
Walker: Lockheed Engineering & Sciences Company, Hampton, VA; Covell and Forrest: Langley Research Center, Hampton, VA.

12a. DISTRIBUTION/AVAILABILITY STATEMENT
Unclassified–Unlimited

Subject Category 02

12b. DISTRIBUTION CODE

13. ABSTRACT *(Maximum 200 words)*
An experimental investigation of the static longitudinal and lateral-directional aerodynamic characteristics of a generic hypersonic research vehicle was conducted in the Langley Unitary Plan Wind Tunnel (UPWT). A parametric study was performed to determine the interference effects of various model components. Configuration variables included delta and trapezoidal canards; large and small centerline-mounted vertical tails, along with a set of wing-mounted vertical tails; and a set of model noses with different degrees of bluntness. Wing position was varied by changing the longitudinal location and the incidence angle. The test Mach numbers were 1.5 and 2.0 at Reynolds numbers of 1×10^6 per foot, 2×10^6 per foot, and 4×10^6 per foot. Angle of attack was varied from $-4°$ to $27°$, and sideslip angle was varied from $-8°$ to $8°$. Generally, the effect of Reynolds number did not deviate from conventional trends. The longitudinal stability and lift-curve slope decreased with increasing Mach number. As the wing was shifted rearward, the lift-curve slope decreased and the longitudinal stability increased. Also, the wing-mounted vertical tails resulted in a more longitudinally stable configuration. In general, the lift-drag ratio was not significantly affected by vertical-tail arrangement. The best lateral-directional stability was achieved with the large centerline-mounted tail, although the wing-mounted vertical tails exhibited the most favorable characteristics at the higher angles of attack.

14. SUBJECT TERMS
Conical forebody; Delta wing; Canard planform; Wing incidence; Wing longitudinal position

15. NUMBER OF PAGES
122

16. PRICE CODE
A06

17. SECURITY CLASSIFICATION OF REPORT	18. SECURITY CLASSIFICATION OF THIS PAGE	19. SECURITY CLASSIFICATION OF ABSTRACT	20. LIMITATION OF ABSTRACT
Unclassified	Unclassified		

NSN 7540-01-280-5500

Standard Form 298(Rev. 2-89)
Prescribed by ANSI Std. Z39-18
298-102

NASA-Langley, 1993